

Quantitative Imaging of Human Red Blood Cells Infected with *Plasmodium falciparum*

Alessandro Esposito,^{†‡*} Jean-Baptiste Choimet,^{†‡} Jeremy N. Skepper,[‡] Jakob M. A. Mauritz,^{†‡} Virgilio L. Lew,[‡] Clemens F. Kaminski,^{†§} and Teresa Tiffert[†]

[†]Department of Chemical Engineering, and Biotechnology, and [‡]Department of Physiology, Development, and Neuroscience, University of Cambridge, Cambridge, United Kingdom; and [§]School for Advanced Optical Technologies, Erlangen, Germany

ABSTRACT During its 48 h asexual reproduction cycle, the malaria parasite *Plasmodium falciparum* ingests and digests hemoglobin in excess of its metabolic requirements and causes major changes in the homeostasis of the host red blood cell (RBC). A numerical model suggested that this puzzling excess consumption of hemoglobin is necessary for the parasite to reduce the colloid osmotic pressure within the host RBC, thus preventing lysis before completion of its reproduction cycle. However, the validity of the colloid osmotic hypothesis appeared to be compromised by initial conflicts between model volume predictions and experimental observations. Here, we investigated volume and membrane area changes in infected RBCs (IRBCs) using fluorescence confocal microscopy on calcein-loaded RBCs. Substantial effort was devoted to developing and testing a new threshold-independent algorithm for the precise estimation of cell volumes and surface areas to overcome the shortfalls of traditional methods. We confirm that the volume of IRBCs remains almost constant during parasite maturation, suggesting that the reported increase in IRBCs' osmotic fragility results from a reduction in surface area and increased lytic propensity on volume expansion. These results support the general validity of the colloid osmotic hypothesis, settle the IRBC volume debate, and help to constrain the range of parameter values in the numerical model.

INTRODUCTION

Plasmodium falciparum parasites are responsible for severe malaria in humans. During their ~48 h asexual reproduction cycle within red blood cells (RBCs), these parasites cause major changes in the homeostasis of the host cell. The glycolytic rate increases by two orders of magnitude (1) and a large fraction of glycolysis-derived energy is invested by the parasite to ingest and digest up to 80% of the host hemoglobin (Hb) and to prevent oxidative damage derived from the associated production of heme (2). Yet, only a small fraction of the amino acids produced are used by the parasite for de novo protein synthesis; the rest is discharged from the infected cell as waste, in what appears to be a squandering of metabolic energy (3). The parasite also permeabilizes the host cell plasma membrane to a variety of ions, nutrients, and waste products by the activation or induction of new permeation pathways (NPPs) of broad substrate selectivity (4,5). Comparably permeabilized, uninfected RBCs have been shown to swell and burst before completion of the 48 h parasite asexual cycle (6), leaving open the question of how infected RBCs, with a growing parasite inside, can reach schizogony without rupturing prematurely.

A mathematical model of the homeostasis of infected RBCs (IRBCs) was developed in an attempt to explain these puzzling observations (7,8). Simulations with the model led

to the suggestion that excess Hb consumption is necessary to reduce the colloid osmotic pressure within the host, and hence the rate of terminal IRBC swelling, thus preventing premature lysis. An attractive feature of the colloid osmotic hypothesis is that it provides a unifying explanation for both excess Hb consumption and premature lysis resistance. However, its validity appeared to be compromised by initial conflicts between model predictions and experimental observations (9,10).

The two critical and controversial model predictions were that 1), the host Hb concentration, not only the Hb content, would decrease progressively during the second half of the asexual reproduction cycle; and 2), the volume of the infected cell would approach its critical hemolytic (spherical) volume (CHV) toward the end of the cycle (7,8). Recent results settled the Hb concentration controversy by confirming the predicted decrease through the independent application of two different imaging methodologies on living cells from *falciparum* cultures (11,12). The second prediction, as originally formulated (7), appeared to conflict with measurements of IRBC volumes that showed little or no increase late in the parasite cycle (10,11,13,14). These volume estimates were also at odds with osmotic fragility measurements that showed a progressive increase in IRBCs with late-stage parasites, suggesting a gradual proximity of the IRBCs to their maximal spherical volume or CHV (7,8). Moreover, studies on the egress process of merozoites suggested a prerupture terminal state of the infected cell with a near-spherical configuration (15). So here we are faced with an apparent conflict between volume measurements suggesting

Submitted November 23, 2009, and accepted for publication April 20, 2010.

*Correspondence: ae275@cam.ac.uk

Alessandro Esposito's present address is Hutchison/MRC Research Centre, Cambridge, United Kingdom.

Editor: Joshua Zimmerberg.

© 2010 by the Biophysical Society
0006-3495/10/08/0953/8 \$2.00

doi: 10.1016/j.bpj.2010.04.065

little change, and osmotic fragility measurements suggesting progressive proximity of IRBCs to their critical hemolytic volume. How can these apparently contradictory findings be reconciled?

One possible explanation is that the membrane area of IRBCs with late-stage parasites is progressively reduced, with a concomitant reduction in critical hemolytic volume. But here again, the evidence for loss of membrane area is inconsistent (16–18). There is a clear need to settle this issue and, to that end, develop a novel methodology that can deliver reliable volume-area estimates of live cells from *falciparum* cultures.

In this work, we developed and applied a much-improved imaging protocol and processing algorithm specifically designed to meet the challenges posed by the complex and continuously evolving shapes of IRBCs. Our goal was to obtain measurement data from single, live cells investigated under optimal physiological conditions that are precise and statistically significant. We developed a robust algorithm to generate three-dimensional (3D) isosurfaces that are elastically deformed until an optimal fit to the cell-to-background transition in the images is found. The isosurface thus generates object contouring with subpixel resolution and permits robust volume-area estimations. Application of this fit-assisted isosurfacing (FAIS) algorithm to IRBC imaging showed that the volume of IRBCs varied little during the parasite's reproductive cycle, but the membrane area loss was significant. The implications of these findings for the colloid-osmotic hypothesis and our understanding of the homeostasis of *falciparum*-infected cells are discussed.

MATERIALS AND METHODS

Chemicals and solutions

All chemicals used in this study were of analytical reagent quality. Calcein-AM was obtained from Invitrogen Ltd. (Paisley, UK). Plasmagel was obtained from Bellon (Neuilly Sur Seine, France). EGTA, Hepes, glucose, inosine, pyruvate, dimethyl sulfoxide (DMSO), RPMI 1640 medium, gentamicin sulfate, glutamine, bovine serum albumin (BSA), ultra-low-gelling-temperature agarose (Sigma Type IX), and all common salts were obtained from Sigma-Aldrich (Gillingham, UK). The human blood and serum used in the cultures were provided by the National Blood Service (UK). Solution A contained (in mM) NaCl, 145; KCl, 3; Na-Hepes (pH 7.5 at 37°C), 10; MgCl₂, 0.15. Solution AE was solution A plus 0.1 mM Na-EGTA. Solution AIP was solution A plus 5 mM inosine and 5 mM pyruvate. Calcein-AM was used as a stock solution of 0.7 mM in DMSO. The stock solution of free calcein was 10 mM in DMSO. Agarose was dissolved at 2% (w/v) in solution AE on the day of use.

Cultures

Two *P. falciparum* clones (ITO4 and A4BC6, kindly provided by B.C. Elford, Institute of Molecular Medicine, Oxford, UK) (19) were cultured separately in human erythrocytes under a low-oxygen atmosphere by standard methods (20). The culture medium was RPMI 1640 supplemented with 40 mM Hepes, 25 mg/L gentamicin sulfate, 10 mM D-glucose, 2 mM glutamine, and 8.5% (vol/vol) pooled human serum. Parasite development and replication were assessed in cultures by microscopic examina-

tion of Giemsa-stained thin blood smears, as previously described (21). Parasitized RBCs were harvested from asynchronous cultures immediately before experiments were initiated. Because the aim of the study was to measure the volume of the cells as close to their original conditions in culture as possible, it was important to establish which procedure would best ensure such an outcome. Therefore, preliminary experiments were performed to establish that the protocols employed did not significantly alter parasite viability (described further below).

Calcein loading

Cells from a *P. falciparum* culture sample were washed once by centrifugation (400 g × 5 min) and resuspension in 10–20 volumes of solution AIP, and the washed cells were suspended at ~2% hematocrit (Hct) in the same solution. A 1–2 mL aliquot of this cell suspension was mixed with calcein-AM stock to a final concentration of ~120 μM in the suspension and incubated at 37°C for 20 min. Inosine in the medium was used as a glycolytic substrate, and pyruvate was used to bypass the glycolytic block generated by the release of formaldehyde during the breakdown of the acetoxymethyl ester that remains fully retained by the cells (22,23). After incubation, the cells were washed twice with solution AIP and the final pellet was diluted 10-fold in AIP medium. One microliter of this cell suspension was gently mixed with 50 μL of the agarose solution (see above) on the surface of a glass culture dish (#1.0; MatTek, Ashland, MA). The culture dish was incubated for 3 min at 4°C to allow gelling, and immediately thereafter was covered with 100 μL of solution AE with 1% BSA, at room temperature, to prevent dehydration of the IRBC-gel mixture during imaging. Preliminary trials showed that gel hydration was essential to prevent cell dehydration, and the presence of BSA was necessary to prevent large-scale crenation of both normal and infected cells. The immobilized cells were allowed to settle for ~10–15 min on the microscopy stage and subsequently were imaged for a maximum of 30 min at room temperature (~20°C), allowing imaging of four to six fields per sample. Repeated volume measurements over the same cell showed no detectable changes in volume during this period. Beyond 30 min, both uninfected and infected cells showed progressive signs of deterioration, such as increased frequency of spontaneous lysis and shape changes.

The images obtained after these procedures systematically rendered normal cell shapes, areas, and volumes for uninfected RBCs and ring-stage-infected RBCs. Bright-field images of calcein-loaded IRBCs with late-stage parasites, obtained from within the agarose gel were consistent with the variety of IRBC shapes reported previously for *falciparum* cultures. The protocol applied was therefore considered to cause minimal perturbation and to be best suited for 3D imaging of living IRBCs.

A critical point in the early stages of this investigation was to set clear selection criteria for trophozoite and schizont stages. Trophozoite-stage IRBCs were selected as those showing a clear food vacuole with visible hemozoin crystals in Brownian motion; these structures were clearly identified in both fluorescence and transmission images (see Fig. 4 C). Mature trophozoite-schizont-stage IRBCs were those with hemozoin crystals compacted into a residual body configuration, with clear evidence of incipient or advanced parasite division within a highly deformed host cell (see Fig. 4, D and E). Preliminary experiments showed that IRBCs exposed to the procedures outlined above for calcein loading and imaging were able to sustain parasitemias near control levels on further culture, indicating that a substantial fraction of the imaged cells were viable. No differences could be detected between the microscopic appearance of unfixed cells immediately out of the culture and those embedded in the agarose gel. Preliminary experiments showed that membrane staining with biotinylated RBC membrane and streptavidin-coated quantum dots or with the membrane probe FM-4-64 did not provide as good a signal/noise ratio (SNR) for volume measurements as calcein, for different reasons. Membrane labeling by sublytic concentrations of quantum dots proved deficient, and FM-4-64 photobleached too rapidly within the acquisition time required for 3D imaging.

Microscopy

Images were acquired with a Leica SP5 AOBS confocal microscope (Leica UK, Milton Keynes, UK) using an HCX PL APO 63.0x1.20 WATER UV water immersion objective (Leica UK). Calcein was excited with the 488 nm laser line and fluorescence was collected over the 500–560 nm band. Bright-field images were collected with the transmission detector. Typically, images were acquired with an x - y pixel resolution of 50 nm, with a separation between optical sections of 150 nm and with a 1 Airy-disk pinhole. Images were then restored (24) with Huygens (SVI, Hilversum, NL) and analyzed with in-house-developed MATLAB software (The MathWorks, Natick, MA). The code for volume estimation of convex polyhedra was adapted from code distributed by Dr. John Burkardt under the GNU LGPL license. Diffusion filtering was performed with the MATLAB nonlinear diffusion toolbox developed by Dr. Federico D'Almeida and distributed under the BSD license.

Rendering and quantification of volumes

Quantitative evaluation of cell volume from fluorescence images depends critically on a correct estimate of the background-to-object transition along the surface of the object whose volume is being measured. The usual assignment of arbitrary threshold isovalues for the transition is prone to error. To eliminate the dependence of the volume estimate on the isovalue, we used the isosurface only as an initial guess for an iterative algorithm (FAIS) that elastically deformed the isosurface according to locally normalized thresholds. At a number of randomly selected vertices of the isosurface, a fluorescence profile was computed along the normal to the object. The curve describing the transition profile along each normal direction was fitted by an error function. For the data shown in this work, the background-to-object transition was set at the inflection point of the fitted sigmoid. The entire initial surface was deformed by interpolation moving the analyzed vertices to their respective inflection points. With confocal images of RBCs, the best results were obtained with a first cycle of optimization selecting 2^5 vertices and a second iteration cycle using 2^7 vertices. Additional details on the algorithm, its software implementation, and simulations are provided in the [Supporting Material](#). The MATLAB code can be freely downloaded from the authors' websites.

RESULTS

Confocal microscopy

Infected and uninfected RBCs from the same culture were loaded with calcein and imaged by confocal laser scanning

microscopy. Serial sections of live cells embedded in low-gelling-temperature agarose are shown in [Fig. 1](#). Deconvolved images are shown with no image enhancements other than color-coding of the fluorescence intensities for easy visualization. [Fig. 1 A](#) shows an uninfected RBC. The normal biconcave shape is apparent from the smooth boundaries of the image and from the doughnut-shaped lower and higher optical slices. [Fig. 1 B](#) shows an RBC containing a ring-stage parasite, and [Fig. 1, C and D](#), show IRBCs with trophozoite-stage and schizont-stage parasites, respectively. The distribution of calcein in the infected cells ([Fig. 1, B and D](#)) is markedly heterogeneous, with intense staining of parasite structures. Calcein appears strongly associated with parasite membranes and with parasite-derived material incorporated in the host cell membrane, as can be seen by the peripheral dotted pattern in [Fig. 1, C and D](#). At this stage, the IRBC has lost its original biconcave shape and presents an irregular surface contour. [Fig. S1](#) shows a merozoite attached to a healthy RBC before invasion.

In [Fig. 1 D](#), calcein fluorescence appears associated with parasite structures that clearly identify a mature parasite stage, such as parasitophorous membrane clefts within the host cytosol. The parasite appears small and compact, and may be in a very early stage of schizogony. To interpret this and similar rendered images of IRBCs with mature parasites, it is important to bear in mind the following points: In contrast to calcein contained within the host cell compartment, the calcein associated with nonmembranous parasite structures tends to photobleach rapidly during the acquisition of 3D image stacks, with fast recovery thereafter, making the parasite appear less bright in the stacked images than when observed under the microscope before or after the data-acquisition interval. Calcein fluorescence was elicited by excitation at 488 nm, and emission was recorded between 500 and 560 nm. Under the experimental conditions applied here, hemozoin autofluorescence excited at 488 nm was largely masked by the bulk fluorescence of calcein, and thus the position of the food vacuole, which is clearly visible

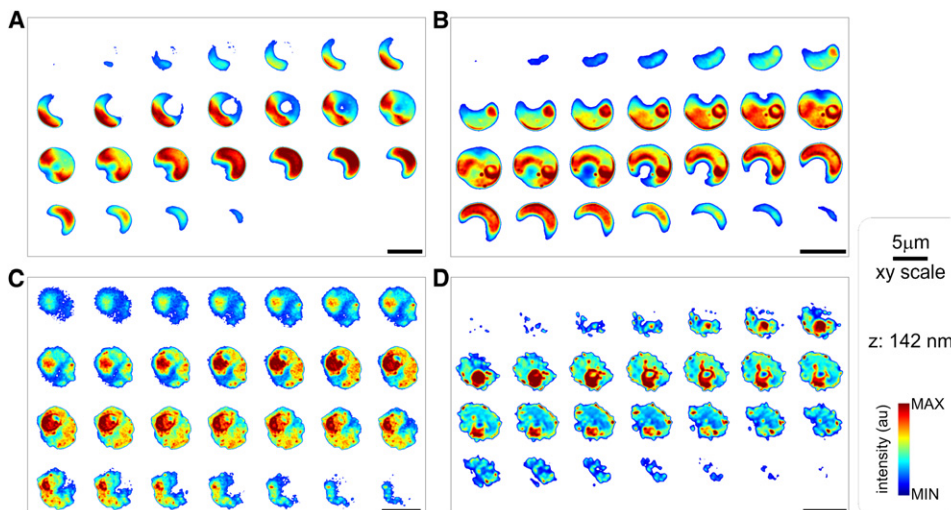


FIGURE 1 Confocal imaging of calcein-loaded infected and uninfected (cohorts) RBCs from the same culture: (A) cohort RBC, (B) IRBC with ring-stage parasite, (C) IRBC with trophozoite-stage parasite, and (D) IRBC with schizont-stage parasite. Images are representative of 119 cells analyzed. Scales are shown in the right panel.

in the transmission images (see Fig. S3 A), remained hardly detectable in the stacked images. A general caveat to consider when analyzing images composed over brief data-acquisition time spans is that the viability of any particular IRBC cannot be fully ascertained. The normal continuity of cultures from calcein-loaded cells established previously (12) is a statistical measure and cannot be interpreted to mean that every cell under observation will experience normal merozoite egress and deliver a full complement of infective merozoites.

Volume reconstruction

Several stereological techniques are available for estimating cell volumes from optical sections, all of which, to a variable degree, depend on a threshold-decision process to define the contour of the object (25,26). Isosurfacing, for instance, depends on the arbitrary selection of a threshold value for the contour of the surfaces to be visualized, causing significant variations in the volume estimates. On the other hand, isosurfacing-based techniques are very useful for representing the 3D morphology of the object. To retain this advantage, and also to be able to apply isosurfacing to estimate both the area and volume of IRBCs, it was necessary to develop a new unsupervised algorithm for surface rendering that circumvents threshold-derived artifacts arising from the large-intensity heterogeneities from IRBCs imaged with fluorescent stains.

Fig. 2 illustrates the effects of noise and the point spread function (PSF) of the microscope on the localization of a 1D boundary. We tested different algorithms on computer-generated data (Fig. 2, B and D, gray circles) using a segment of known length (Fig. 2 B, d) after applying a Gaussian PSF to a step function in the absence or presence of noise (Fig. 2, C and D, respectively). It can be seen that the length of the segment can be approximated by the distance between the inflection points of the sigmoid functions used to fit the transition from background to the fluorescent object.

Fig. 3 illustrates a comparison between the fit-assisted (FA) algorithm developed here and the gradient-based (GB) methods used to estimate the object-to-background transition. Traditional GB techniques rely on the analysis of gradients after smoothing with a Gaussian kernel (MAXD1 technique (27); blue curves) or after diffusion filtering (adaptive (28,29); green curves). The SNR (x axis) is the total number of photons generated in a computer-simulated data set like the one used for Fig. 2. The lines in Fig. 3 A compare the precision with which the FA and GB methods estimate the length of an object. The coefficient of variation (CV) of the segment length was normalized with Poissonian noise (i.e., the inverse of the square root of the number of collected photons). It can be seen that the normalized CV of the FA-computed algorithm remains optimized at all SNRs, whereas that of the GB algorithms increases with SNR and thus decreases in relative efficiency at higher

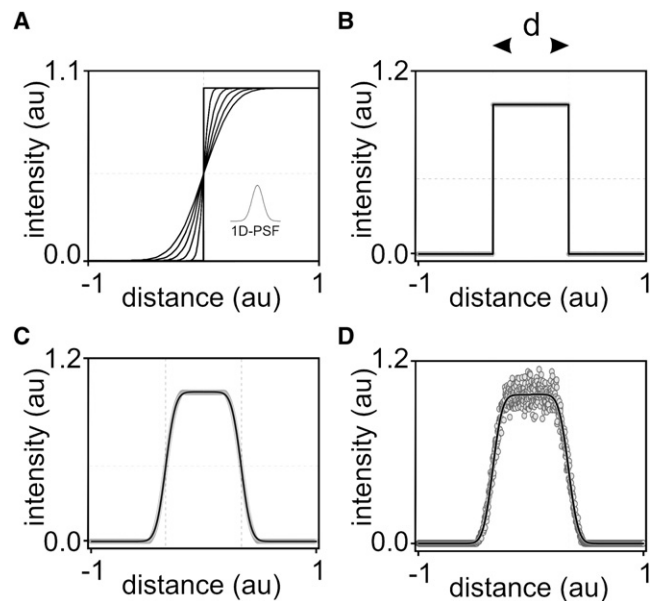


FIGURE 2 Background-to-object transition and length estimates obtained with the FA algorithm. The procedure is illustrated with a 1D example using simulated fluorescent intensity versus distance diagrams; intensity and distance are expressed in arbitrary normalized units (au). (A) Background-to-object transition. The PSF of the microscope smooths the sharp simulated background-to-object transition to an extent determined by the SD of the error function, illustrated here for values between 0 (steepest slope) and 1 (shallowest slope), in arbitrary normalized units. In panels B–D, boundary transitions to an object of length d are generated from computer simulations and are represented by gray circles; in panels B and C, the gray circles overlap and result in a gray outline. The continuous curves represent the fit obtained with the fitting algorithm. (B) Sharp transition. (C) With blurring. (D) With blurring and noise.

SNR values. The FA method offers improved efficiency because it uses the full information content of the data set, whereas GB methods use only the photons in the neighborhood of the boundary.

Optimal precision for segment length is approached at sufficiently high SNR (Fig. 3, B and C). Given the pixelated nature of the images, optimal resolution with the FA method is achieved with $\sim 10^3$ photons, whereas the GB methods require $>10^6$ photons for an equivalent resolution of object length (Fig. 3 C, asterisk). Moreover, the FA algorithm can deliver subpixel resolution for both the absolute position of the object boundaries and for measurement of object length (Fig. 3, B and C, respectively, dashed red lines). We tested this by positioning the object transition in the middle of two sample pixels and plotting the FA results without rounding up the values to the nearest pixel.

Fig. 3 D shows numerical volume estimates on synthetic data as a function of sample number (see the Supporting Material for further details). We analyzed 75 synthetic objects generated by simulations in the presence of noise by applying an increasing threshold for isosurfacing (from 15% to 30% of the maximum intensity value), which resulted in a decrease of the volume estimates (Fig. 3 D, blue curve).

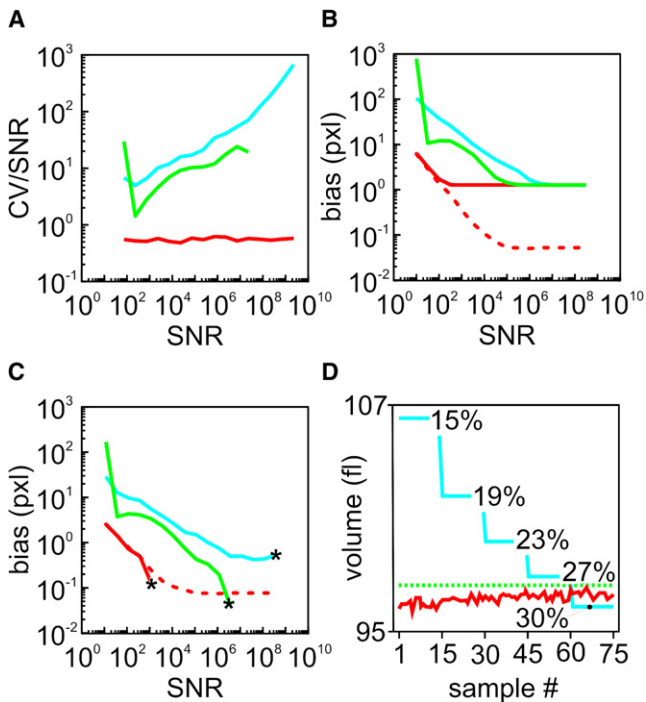


FIGURE 3 Comparison between the FA algorithm and GB methods for estimating the object-to-background transition and object volume. Panels A–C compare efficiencies in boundary estimates as a function of the SNR of the data set; efficiency is reported as the ratio of the CV to the SNR. Note that lower values equal better performance. In panel D, estimated volumes (in fL) are reported as a function of the number of synthetic objects simulated (sample number). Color codes: red (*lower curve*), FA algorithm; blue (*upper curve*), gradient filtering; green (*middle curve*), diffusional filtering. Dashed segments stress the superior precision of the FA algorithm for subpixel resolution. (A) Statistical error in length estimation normalized by Poissonian noise. (B) Bias in the estimate of the absolute position of the boundary. (C) Bias in the estimate of the length of the simulated segment. (D) Comparison of volume estimates on 75 different simulated 3D samples by the FA algorithm (*red, lower curve*) and GB isosurface rendering (*blue, upper curve*) at different isovalues from 15% to 30% of the maximal intensity. The dashed green line indicates the actual volume of the simulated object. Note that the FA algorithm approximates the simulated volume better than the GB methods at all initial threshold values.

On the other hand, the FAIS algorithm (*red curve*) rendered values close to the set true value (*green dotted curve*) at all initial thresholds. Fig. S2 illustrates the robustness of this approach in a 3D rendering of highly irregular objects.

Morphology and volume and area estimates of IRBCs

Cohort RBCs (healthy RBCs from the same culture as the IRBCs) and cells infected with parasites at different stages of development were imaged and analyzed using the FAIS algorithm. The results of representative transmission and fluorescence confocal images, together with the 3D images reconstructed using the FAIS algorithm, are shown in Fig. 4. The cohort RBCs exhibit the typical biconcave shape (Fig. 4 A) and are not much perturbed at the ring stage

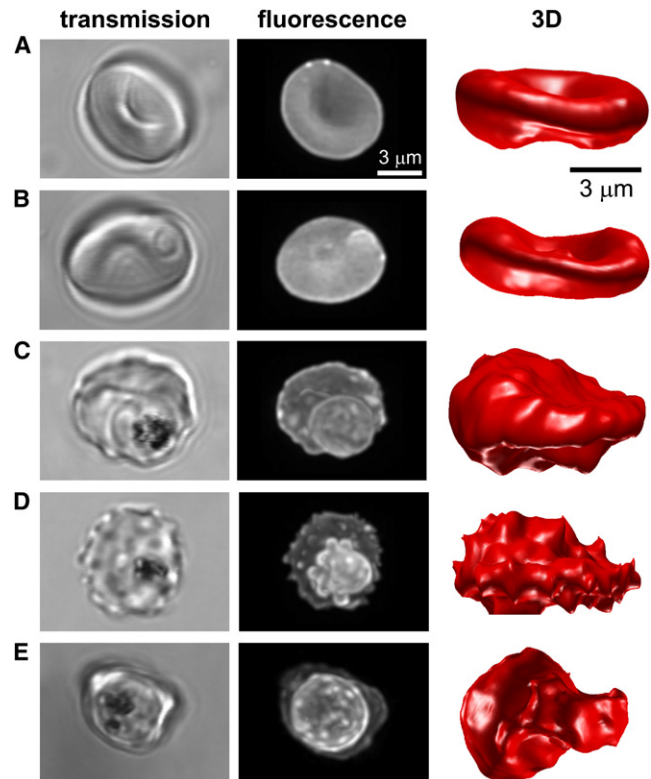


FIGURE 4 Transmission, confocal, and 3D images of a cohort cell (A), ring-stage IRBC (B), trophozoite-stage IRBC (C), and schizont-stage IRBC (D and E). Fluorescence images are maximum intensity projections of the deconvolved confocal 3D image stacks. The selected images are representative of a total of 119 cells analyzed. Panels D and E show typical phenotypes exhibited by schizont-infected RBCs.

(Fig. 4 B). At the trophozoite and schizont stages (Fig. 4, C–E), the IRBCs show progressive surface deformations with irregular bulges. The spiky appearance of the surface (Fig. 4 D) in ~60% of the calcein-reconstructed images is a software-rendered 3D interpretation of the membrane bulges and irregularities that are clearly visible in the corresponding transmission images and fluorescence projections (Fig. S3 A). At the optical resolution of the confocal microscope, the fine structure of the bulges is not resolved. Those that appear as spikes may correspond to the membrane projections that are more clearly seen in serial sections obtained at electron-microscopy resolution (illustrated in Fig. S3 B (30,31)). A fraction of such membrane projections and folds may represent a small reservoir of membrane area that is undetectable at optical-microscopy resolution. What is clear is that the spikes do not reflect classic surface crenations and cannot be described as such.

Volume estimates were obtained from a total of 119 cells (44 cohorts and 75 IRBCs) and the results, normalized to the mean of the uninfected cohorts, are shown in Fig. 5 A. In this figure, the volume histogram is superimposed on model simulations for comparisons between measured values and model predictions (analyzed in the Discussion section).

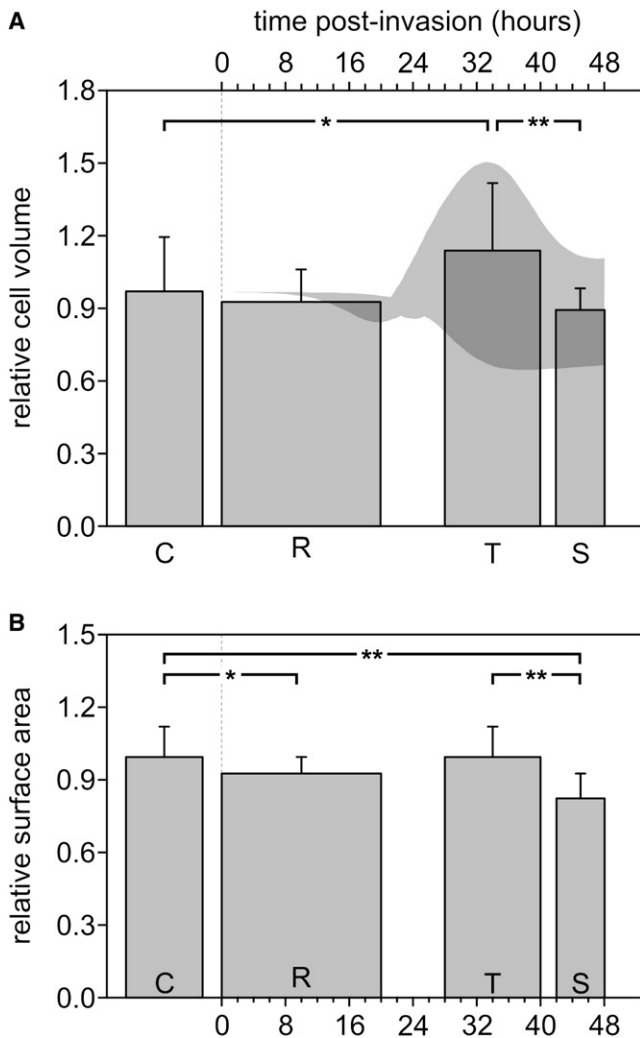


FIGURE 5 Volume and area estimates of IRBCs with parasites at different stages of development. Volume (A) and area (B) values are normalized to the corresponding means in the uninfected cohort RBCs. The columns report the mean \pm SD. Column width reflects the probable time interval for each parasite developmental stage as selected by the criteria described in **Materials and Methods**. R: rings; T: trophozoites; S: schizonts. Horizontal lines above the columns report the statistical significance of differences between indicated groups (* $p < 0.01$, ** $p < 0.001$). The shadowed area in the top graph reports a subset of data from the malaria model (9), the significance of which is analyzed in the Discussion section.

The variation in normalized results is reported as the standard deviation (SD) instead of the standard error of the mean because the statistical variation encompasses some asynchrony in the choice of imaged cells to represent each developmental stage and natural phenotypic polymorphisms, as well as measurement noise. Therefore, any difference of minor statistical significance has no value in such a sample.

The actual volume of the uninfected cohort RBCs was 88 ± 20 fL (mean \pm SD), well within the range for normal human RBCs. The volume of all cells relative to the cohort mean was as follows (mean \pm SD, n = number of cells): cohorts, 1.00 ± 0.22 , $n = 44$); ring-stage IRBCs, $0.94 \pm$

0.14 , $n = 19$; trophozoite-stage IRBCs, 1.17 ± 0.29 , $n = 42$; and schizont-stage IRBCs, 0.92 ± 0.09 , $n = 14$. The statistically significant differences were a 17% increase in volume between uninfected RBCs and trophozoites ($p < 0.01$, t -test) and a 22% volume reduction between trophozoite- and schizont-stage parasites ($p < 0.001$).

The surface area of cohort RBCs was $120 \pm 15 \mu\text{m}^2$. The relative area estimates on all cell samples were (mean \pm SD, relative to cohorts) 1.00 ± 0.12 for cohorts, 0.92 ± 0.07 for ring-stage IRBCs, 0.99 ± 0.12 for trophozoite-stage, and 0.82 ± 0.11 for schizont-stage IRBCs (the difference between the last two was statistically significant: $\sim 18\%$; $p < 0.001$).

DISCUSSION

The aim of this study was to provide a reliable quantitative estimate of the volume and area of RBCs infected with single *P. falciparum* parasites at different developmental stages. The results show that the volume of IRBCs remains within a narrow margin of variation relative to that of uninfected cohorts throughout the reproduction cycle of the parasite, confirming earlier results by Allen and Kirk (10), Saliba et al. (14), Elliot et al. (13), and Park et al. (11). The main statistically significant differences were found between the trophozoite and schizont stages (Fig. 5), amounting to a volume reduction of $\sim 22\%$ and an area reduction of $\sim 18\%$. We comment next on the methodological innovations that were deemed necessary to achieve satisfactory results, and analyze their significance.

The FAIS algorithm we developed and applied here allows quantification of volume and surface area, eliminating the user- and threshold-dependent biases that arise in analyses of heterogeneous irregular objects with other methodologies. Furthermore, the algorithm enables object boundaries to be fit at subpixel resolution (Fig. 3, B and C). With this level of precision (Fig. 3), the observed variations in volume and surface area can confidently be attributed to genuine variations in phenotype and developmental stage. These variations are relatively large, with CVs ranging from 10% to 25% for volumes, and from 8% to 13% for areas (Fig. 5). Below, we consider how our results can be used to clarify the volume-area controversies in relation to the colloid-osmotic hypothesis.

As previously noted (7,8), the increasing osmotic fragility of IRBCs with late-stage parasites reflects a predisposition of IRBCs to lyse upon rapid volume expansion. If, as confirmed by the results presented here, the volume of IRBCs within the range of observed variation remains confined well below the critical hemolytic volume of uninfected cells, then either the membrane area will be reduced or the membrane structure will be altered. Then, upon volume expansion during osmotic fragility measurements, the membrane permeability barrier will become disrupted before the cell attains its maximal spherical configuration, or both. Our

results suggest that there is a significant loss in membrane area, averaging 18%, between the trophozoite and schizont stages (Fig. 5 B), supporting earlier estimates of late membrane area losses (18). It is worth pointing out, however, that our estimate represents an upper limit by this method because the measurements cannot detect submicroscopic membrane folds constituting a potential reservoir of membrane area.

Let us consider the extent to which even the maximal estimated area loss might account for the observed increase in osmotic fragility. A fractional reduction f in the membrane area of a cell will reduce its maximal spherical volume by $(1 - f)^{3/2}$, amounting to a mean reduction in critical hemolytic volume of ~26% for $f = 0.18$. Could membrane area loss fully account for the large increase in osmotic fragility of IRBCs with late-stage parasites? Approximate estimates (see Supporting Material) suggest that an 18% area loss may account for osmotic fragility shifts of up to ~0.7 relative tonicity, a substantial increase over the 0.45–0.50 mean value for uninfected RBCs. However, significant fractions of late-stage IRBCs lyse at relative tonicities of 0.8–0.9 (8). Therefore, although membrane area loss may be an important contributor to the observed increase in osmotic fragility, it is very likely that structural membrane alterations also play an important role. We may therefore conclude that the increased proximity of IRBCs to a critical hemolytic volume exposes a progressive vulnerability to lysis by volume expansion; this is then counteracted by the reduction in osmolyte concentration within the host cell cytosol resulting from excess hemoglobin consumption. Proximity to the CHV, rather than the actual volume of the IRBCs, is thus the critical condition for the validity of the colloid osmotic hypothesis.

We consider next the relevance of these results as regards our understanding of IRBC homeostasis. The shaded area in Fig. 5 A frames the results of simulations using the IRBC homeostasis model with a subset of parameters selected to best fit the observed volume variability (see Supporting Material). This subset constrains the range of likely homeostatic parameter values during the asexual reproduction cycle of IRBCs with single parasites. The defining parameter of this subset, with a value of 0.3, is the coupling factor that relates parasite volume growth to hemoglobin consumption (9), and renders mature parasites volumes in the 30–50 fL range, in agreement with previous results (11,13,14). With this value for the coupling factor, the shaded area in Fig. 5 A covers variations in the half-times for NPP development and hemoglobin consumption of 27 ± 5 and 32 ± 6 h, respectively, corresponding to the experimentally reported values for a ± 1 SD statistical variation in these parameters (9). These variations may be reinterpreted as reflecting genuine heterogeneity in parasite development under the conditions of the culture from which the analyzed samples were harvested. A salient feature of the shaded profile in Fig. 5 A is the biphasic volume pattern apparent in the top outline.

The results support a statistically significant reduction in IRBC volume of ~22% between the trophozoite and schizont stages. The model parameters that conform with that profile generate a sequence in which the large, early NaCl and water gains incurred by the host after NPP development are followed by a volume decrease due to late hemoglobin consumption exceeding the late NaCl and water gains at a stage when sodium gradient dissipation has minimized the driving force for further net NaCl influx.

In conclusion, the results presented here, which were obtained using a new algorithm for the quantitative measurement of volume and surface area of irregularly shaped cells, show that the volume of *falciparum*-parasitized RBCs varies little from that of uninfected RBCs (11,13,14). The direct, noninvasive volume measurements of IRBCs agree well with the volume predictions of the IRBC homeostasis model corrected down for realistic parasite volumes (32). This work resolves the conflict between earlier volume estimates (8,10) and adds further support to the view that the increase in osmotic fragility of IRBCs with late-stage parasites can be attributed to both a reduction in the host-cell membrane area and an increased vulnerability to prespherical lysis upon volume expansion.

SUPPORTING MATERIAL

Six figures are available at [http://www.biophysj.org/biophysj/supplemental/S0006-3495\(10\)00600-4](http://www.biophysj.org/biophysj/supplemental/S0006-3495(10)00600-4).

This work was supported by funds from the Engineering and Physical Sciences Research Council (EP/E059384) and the Biotechnology and Biological Sciences Research Council (BB/E008542/1), and by a grant from the Isaac Newton Trust to T.T. A.E. is funded by the Engineering and Physical Sciences Research Council (EP/F044011/1).

REFERENCES

1. Kanaani, J., and H. Ginsburg. 1989. Metabolic interconnection between the human malarial parasite *Plasmodium falciparum* and its host erythrocyte. Regulation of ATP levels by means of an adenylate translocator and adenylate kinase. *J. Biol. Chem.* 264:3194–3199.
2. Rudzinska, M. A., W. Trager, and R. S. Bray. 1965. Pinocytotic uptake and the digestion of hemoglobin in malaria parasites. *J. Protozool.* 12:563–576.
3. Krugliak, M., J. Zhang, and H. Ginsburg. 2002. Intraerythrocytic *Plasmodium falciparum* utilizes only a fraction of the amino acids derived from the digestion of host cell cytosol for the biosynthesis of its proteins. *Mol. Biochem. Parasitol.* 119:249–256.
4. Ginsburg, H., S. Kutner, ..., Z. I. Cabantchik. 1985. Characterization of permeation pathways appearing in the host membrane of *Plasmodium falciparum* infected red blood cells. *Mol. Biochem. Parasitol.* 14:313–322.
5. Kirk, K. 2001. Membrane transport in the malaria-infected erythrocyte. *Physiol. Rev.* 81:495–537.
6. Staines, H. M., J. C. Ellory, and K. Kirk. 2001. Perturbation of the pump-leak balance for Na(+) and K(+) in malaria-infected erythrocytes. *Am. J. Physiol.* 280:C1576–C1587.
7. Lew, V. L., T. Tiffert, and H. Ginsburg. 2003. Excess hemoglobin digestion and the osmotic stability of *Plasmodium falciparum*-infected red blood cells. *Blood.* 101:4189–4194.

8. Lew, V. L., L. Macdonald, ..., T. Tiffert. 2004. Excess haemoglobin digestion by malaria parasites: a strategy to prevent premature host cell lysis. *Blood Cells Mol. Dis.* 32:353–359.
9. Mauritz, J. M. A., A. Esposito, ..., V. L. Lew. 2009. The homeostasis of *Plasmodium falciparum*-infected red blood cells. *PLOS Comput. Biol.* 5:e1000339.
10. Allen, R. J., and K. Kirk. 2004. Cell volume control in the *Plasmodium*-infected erythrocyte. *Trends Parasitol.* 20:7–10, discussion 10–11.
11. Park, Y., M. Diez-Silva, ..., S. Suresh. 2008. Refractive index maps and membrane dynamics of human red blood cells parasitized by *Plasmodium falciparum*. *Proc. Natl. Acad. Sci. USA.* 105:13730–13735.
12. Esposito, A., T. Tiffert, ..., V. L. Lew. 2008. FRET imaging of hemoglobin concentration in *Plasmodium falciparum*-infected red cells. *PLoS One.* 3:e3780.
13. Elliott, J. L., K. J. Saliba, and K. Kirk. 2001. Transport of lactate and pyruvate in the intraerythrocytic malaria parasite, *Plasmodium falciparum*. *Biochem. J.* 355:733–739.
14. Saliba, K. J., H. A. Homer, and K. Kirk. 1998. Transport and metabolism of the essential vitamin pantothenic acid in human erythrocytes infected with the malaria parasite *Plasmodium falciparum*. *J. Biol. Chem.* 273:10190–10195.
15. Glushakova, S., D. Yin, ..., J. Zimmerberg. 2005. Membrane transformation during malaria parasite release from human red blood cells. *Curr. Biol.* 15:1645–1650.
16. Omodeo-Salè, F., A. Motti, ..., D. Taramelli. 2003. Accelerated senescence of human erythrocytes cultured with *Plasmodium falciparum*. *Blood.* 102:705–711.
17. Nash, G. B., E. O'Brien, ..., J. A. Dormandy. 1989. Abnormalities in the mechanical properties of red blood cells caused by *Plasmodium falciparum*. *Blood.* 74:855–861.
18. Zanner, M. A., W. R. Galey, ..., D. L. Vander Jagt. 1990. Water and urea transport in human erythrocytes infected with the malaria parasite *Plasmodium falciparum*. *Mol. Biochem. Parasitol.* 40:269–278.
19. Berendt, A. R., D. L. Simmons, ..., K. Marsh. 1989. Intercellular adhesion molecule-1 is an endothelial cell adhesion receptor for *Plasmodium falciparum*. *Nature.* 341:57–59.
20. Trager, W., and J. B. Jensen. 1976. Human malaria parasites in continuous culture. *Science.* 193:673–675.
21. Tiffert, T., H. M. Staines, ..., V. L. Lew. 2000. Functional state of the plasma membrane Ca^{2+} pump in *Plasmodium falciparum*-infected human red blood cells. *J. Physiol.* 525:125–134.
22. Tiffert, T., J. Garcia-Sancho, and V. L. Lew. 1984. Irreversible ATP depletion caused by low concentrations of formaldehyde and of calcium-chelator esters in intact human red cells. *Biochim. Biophys. Acta.* 773:143–156.
23. García-Sancho, J. 1985. Pyruvate prevents the ATP depletion caused by formaldehyde or calcium-chelator esters in the human red cell. *Biochim. Biophys. Acta.* 813:148–150.
24. Difato, F., F. Mazzone, ..., A. Diaspro. 2004. Improvement in volume estimation from confocal sections after image deconvolution. *Microsc. Res. Tech.* 64:151–155.
25. Fang, S. F., Y. Dai, ..., K. Dunn. 2000. Three-dimensional microscopy data exploration by interactive volume visualization. *Scanning.* 22: 218–226.
26. Kubínová, L., J. Janáček, ..., Z. Opatrný. 1999. Comparison of several digital and stereological methods for estimating surface area and volume of cells studied by confocal microscopy. *Cytometry.* 36:85–95.
27. Sieracki, M. E., S. E. Reichenbach, and K. L. Webb. 1989. Evaluation of automated threshold selection methods for accurately sizing microscopic fluorescent cells by image analysis. *Appl. Environ. Microbiol.* 55:2762–2772.
28. Tabik, S., E. M. Garzon, ..., J. J. Fernandez. 2007. High performance noise reduction for biomedical multidimensional data. *Digit. Signal Process.* 17:724–736.
29. Malm, H., G. Sparr, ..., C. F. Kaminski. 2000. Nonlinear diffusion filtering of images obtained by planar laser-induced fluorescence spectroscopy. *J. Opt. Soc. Am. A Opt. Image Sci. Vis.* 17:2148–2156.
30. Lew, V. L., and A. R. Hockaday. 1999. The effects of transport perturbations on the homeostasis of erythrocytes. *Novartis Found. Symp.* 226:37–50, discussion 50–54.
31. Lew, V. L., A. Hockaday, ..., R. M. Bookchin. 1988. Mechanism of spontaneous inside-out vesiculation of red cell membranes. *J. Cell Biol.* 106:1893–1901.
32. Elliott, D. A., M. T. McIntosh, ..., K. A. Joiner. 2008. Four distinct pathways of hemoglobin uptake in the malaria parasite *Plasmodium falciparum*. *Proc. Natl. Acad. Sci. USA.* 105:2463–2468.